Electrochemical modulation enhances the selectivity of peripheral neurostimulation in vivo

Matthew T. Flavin[a,b], Marek A. Paul[c,d], Alexander S. Lim[e], Charles A. Lissandrello[b], Robert Ajemian[e], Samuel J. Lin[c], and Jongyoon Han[a,f,1]

Electrical nerve stimulation serves an expanding list of clinical applications, but it faces persistent challenges in selectively activating bundled nerve fibers. In this study, we investigated electrochemical modulation with an ion-selective membrane (ISM) and whether it, used together with electrical stimulation, may provide an approach for selective control of peripheral nerves. Guided by theoretical transport modeling and direct concentration measurements, we developed an implantable, multimodal ISM cuff capable of simultaneous electrical stimulation and focused Ca^{2+} depletion. Acutely implanting it on the sciatic nerve of a rat in vivo, we demonstrated that Ca^{2+} depletion could increase the sensitivity of the nerve to electrical stimulation. Furthermore, we found evidence that the effect of ion modulation would selectively influence functional components of the nerve, allowing selective activation by electrical current. Our results raise possibilities for improving functional selectivity of new and existing bioelectronic therapies, such as vagus nerve stimulation.

ion-tronic | concentration polarization | electrophoretic drug delivery | neuroprosthesis

The rapidly growing field of bioelectronic medicine relies on direct electrical stimulation for most of its applications in the peripheral nervous system (1). On demand and localized, its use in modalities, such as vagus nerve stimulation (VNS) (2, 3) and functional electrical stimulation (FES) (4) has improved clinical outcomes for an expanding array of neurological disorders. However, peripheral nerves contain bundles of both sensory and motor fibers, each producing distinct and sometimes harmful effects upon activation (5, 6). Selective targeting of individual fibers and the minimization of off-target effects remain challenging for direct electrical stimulation (7). While spatially resolved electrode arrays have yielded improved outcomes for modalities such as VNS and FES (5, 8), invasiveness scales with spatial selectivity (9), and the more invasive interfaces confront long-term stability issues (7).

In this study, we investigated electrochemical modulation—whether this recently introduced modality may be used synergistically with direct electrical stimulation to improve and control its selectivity. Chemical modulation is traditionally delivered through systemic administration of drug compounds (e.g., through oral or intravenous routes). Even without physical localization, circulating agents can target specific populations of cells. The selectivity of a chemical agent arises from intrinsic factors, including its affinity for the target and its transport in the surrounding tissue (10). To leverage both the intrinsic selectivity of chemical modulation and the spatiotemporal resolution of direct electrical stimulation, we employed a local chemical delivery platform as part of our multimodal electronic implant. Previous studies have successfully realized local chemical delivery through a variety of mechanisms, including passive diffusion (11), pressure (12), and electrophoresis (13). As demonstrated by investigators such as Berggren and coworkers (14), electrophoretic delivery with ion-tronic materials permits remote, on-demand, low-latency operation and does not require bulky mechanical components. In a recent work, our group introduced the use of an ion-selective membrane (ISM) as a central component of an ion-tronic delivery system (15).

Ionophore-based ISMs are capable of selectively filtering individual ion species from a mixed electrolyte background. From the concentration-sensing applications for which ISMs were originally developed, numerous carrier-based membranes exist with tunable selectivity for a wide range of ions (16–19). Electrical current applied across the membrane drives the concentration polarization of the selected ion in the electrolyte volumes on either side. A selected ion of positive charge becomes enriched where current leaves the membrane and depleted where current enters (20). Its ability to deplete the targeted ion is singular among local delivery methods. This operation also raises the prospect of remote refilling, drawing ions back into the internal reservoir after a delivery cycle. Here, we provide an in vivo demonstration of an ISM-based device, a fully implantable system designed for the depletion of Ca^{2+} ions in peripheral nerves (Fig. 1).

Significance

Bioelectronic medicine relies on electrical stimulation for most applications in the peripheral nervous system. It faces persistent challenges in selectively activating bundled nerve fibers. Here, we investigated ion-concentration modulation with ion-selective membranes and whether this modality may enhance the functional selectivity of peripheral nerve stimulation. We designed a multimodal stimulator that could control Ca^{2+} concentrations within a focused volume. Acutely implanting it on the sciatic nerve of a rat, we demonstrated that Ca^{2+} depletion could increase the sensitivity of the nerve to electrical stimulation in vivo. We provided evidence that it selectively influenced individual fascicles of the nerve, allowing selective activation by electrical current. Improved functional selectivity may improve outcomes for important therapeutic modalities.
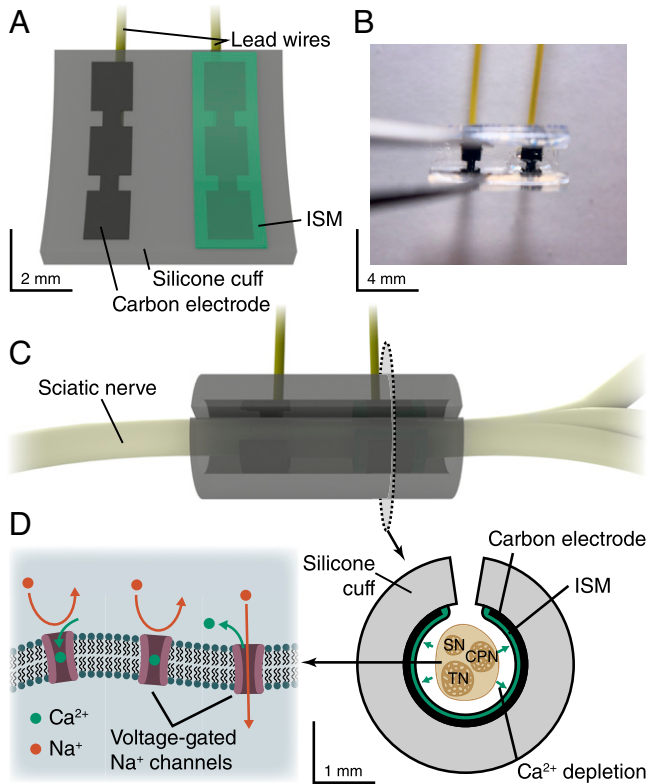
Fig. 1. Depiction of the Ca²⁺-selective ISM-cuff electrode. (*A*) Illustration of the inside surface of the cuff. (*B*) Photograph of one of the devices used in our studies. (*C*) Illustration of the cuff implanted on the sciatic nerve. *Inset* in the lower right shows the cross-sectional area of the ISM-coated electrode contact. The fascicles of the sciatic nerve that diverge into the sural, common peroneal, and tibial nerves are denoted in this diagram as SN, CPN, and TN, respectively. (*D*) Schematic illustration of voltage-gated sodium channels and their interaction with extracellular Ca²⁺.

In our system, the role of Ca²⁺ modulation is to control the effect of electrical stimulation rather than to directly elicit activation on its own. As previously demonstrated, peripheral nerves become sensitized to activation by electrical current under Ca²⁺ depletion and desensitized under enrichment (15, 21). Mechanistically, this manipulation targets voltage-gated sodium channels, which are stabilized by Ca²⁺ as a cofactor under normal conditions (Fig. 1*D*) (22). There exists a natural, intrinsic variation in both the expression of voltage-gated sodium channels (23) and the characteristic transport of ions (24, 25) among functionally distinct fibers of peripheral nerves. Therefore, we predicted that Ca²⁺ depletion would differentially affect unique subsets of those fibers. In our study, we investigated whether local Ca²⁺ depletion would enhance the selectivity of a rat sciatic nerve to electrical stimulation with respect to functionally distinct fibers.

In our previous ex vivo study with the frog sciatic nerve, we demonstrated that a prototypical ISM-based device could deplete Ca²⁺ and in doing so, sensitize the nerve to activation (15). In this study, for our implant to function while embedded in the deep tissue of a rat's gluteal region, we utilized a cuff electrode architecture. Its development was guided by predictions from an electrochemical transport model (26). As verified in this study, the enclosing volume of the cuff's cylindrical lumen focuses the delivery of Ca²⁺ depletion, preventing dissipation into the surrounding tissue. As shown in Fig. 1*A*, the cuff had two contacts: an uncoated electrode that would deliver electrical stimulation and an ISM-coated contact that would perform Ca²⁺ depletion. Along with conventional electrochemical characterization methods, we

studied the multimodal device's operation using a direct sensing technique that we recently developed (27).

Enabled by the ISM-cuff electrode, we carried out an in vivo study of electrochemical modulation in an acute rat sciatic nerve preparation. We used it to investigate the effects of electrochemical modulation in an implanted environment and ultimately, to determine whether Ca²⁺ depletion enables selective electrical excitation. While applying multimodal stimulation through the cuff, we recorded compound muscle action potentials (CMAPs) from the gastrocnemius, tibialis anterior, and biceps femoris. Using these three muscles as indicators for the underlying electrical activity within the fascicles of the sciatic nerve that innervates them, we examined their recordings for evidence of selective modulation.

Results

Operating Principles of a Multimodal ISM Cuff. Recent studies have revealed that intensive currents across an ISM can lead to adverse processes, such as loss of transfer selectivity and leaching of membrane components (27). As part of our study, we investigated these phenomena along with other harmful electrochemical processes that accompany implanted electrodes in the context of our applied ISM-based device.

We fabricated our cuff electrode using an adaptation of the process reported by our group (Fig. 1*B*) (28). Screen-printing carbon–polymer contacts, we produced electrodes with impedances similar to platinum foil—$341 \pm 36.9\,\Omega$ ($n = 6$)—measured by electrochemical impedance spectroscopy (Fig. 2 *A* and *B*). As shown by the chronopotentiogram in Fig. 2*D*, we were able to operate the electrodes at currents of $-20\,\mu A$ for over 300 s while remaining within the electrochemical window between –1 and 1 V. The cyclic voltammogram (Fig. 2*C*) of each electrode was largely rectangular between –1 and 1 V with the onset of some minor features around –0.1 and 0.2 V (29). No gas bubbles were observed during either cyclic voltammetry or chronopotentiometry. These measurements, which remained consistent during mechanical testing, suggest that the electrodes can be operated at $-20\,\mu A$ for 300 s without encountering harmful electrochemical processes, such as electrolysis (*SI Appendix* has an extended discussion).

To understand the behavior of the ISM-coated contact of the cuff, we started by developing a Nernst–Planck–Poisson solute transport model. Adapted from our previous work (26), it reproduces interfacial processes that affect electrically driven transport in ISM systems (*Materials and Methods*). Its parameters were sourced a priori from previous literature rather than by model fitting. Our simulations support the principle of the ISM-based device—the geometry of the cuff focuses Ca²⁺ depletion within its confined volume. For the same magnitude of current, our model showed that this configuration produces a stronger effect than a planar, unconfined electrode. As demonstrated in Fig. 2*E*, the model predicted that applying $-20\,\mu A$ at the ISM-coated contact could reduce the concentration of Ca²⁺ in the center of the lumen from 2 mM to below 0.5 mM over the course of 5 min. Prior studies in the ex vivo frog sciatic nerve indicate that this magnitude and duration of Ca²⁺ depletion would elicit substantive changes in nerve sensitivity (21).

The characteristic volume of Ca²⁺ depletion scales to the geometry of the electrode. For a planar, unconfined electrode, Ca²⁺ depletion reaches steady state at a distance on order of the electrode's radius. Meanwhile, Fig. 2*E* shows that for our confined electrode, Ca²⁺ depletion advances until it scales to the inner diameter of the cuff. For both the confined and unconfined electrodes, the
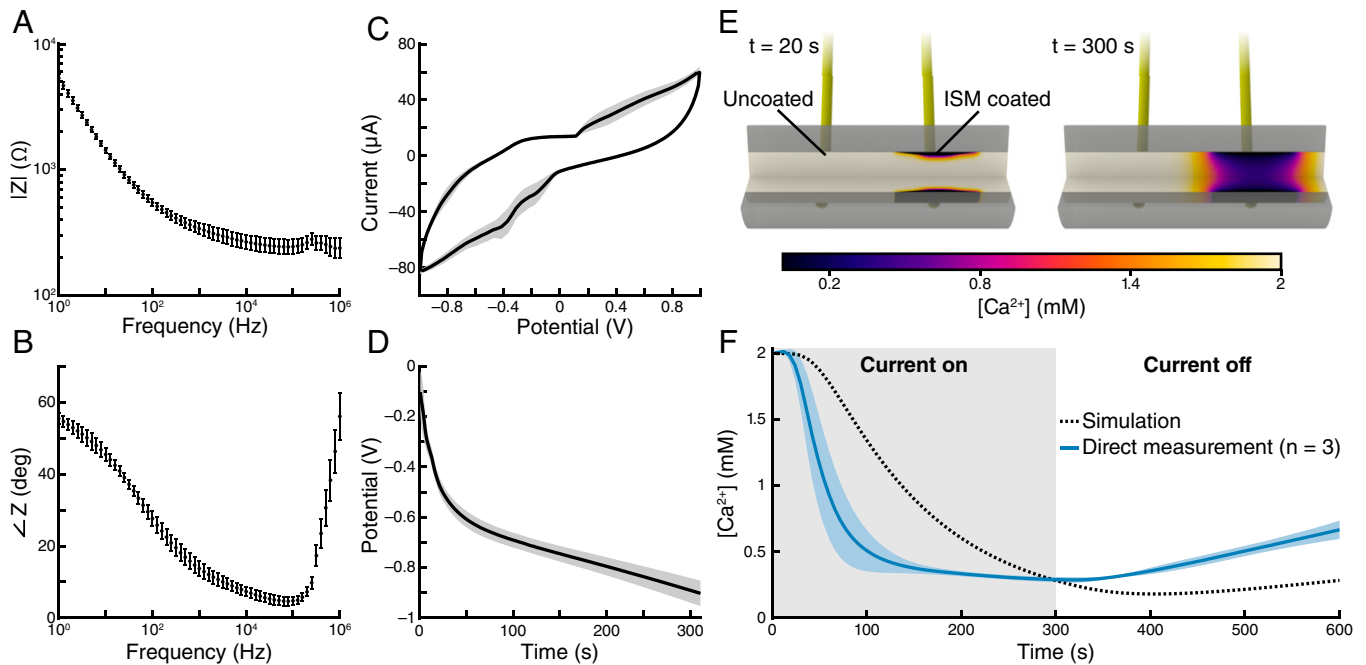
Fig. 2. Study of uncoated and ISM-coated contacts of our multimodal cuff. (*A* and *B*) Magnitude and phase components of the Bode plot for electrochemical impedance spectroscopy applied at the uncoated contact of each cuff. Impedances were measured at 60 frequencies logarithmically spaced between 1 Hz and 1 MHz (10 mV rms, biased to the cell's open-circuit potential; $n = 6$; measured after mechanical testing). (*C*) Cyclic voltammogram of the uncoated contacts scanned at 100 mV s^{-1} between −1 and 1 V ($n = 6$; the shaded region indicates the SD; measured after mechanical testing). (*D*) Chronopotentiogram of uncoated contacts under −20 μA of current ($n = 6$; the shaded region indicates the SD; measured after mechanical testing). (*E*) Numerical results to the Nernst–Planck–Poisson solute transport model at t = 20 s and t = 300 s (applying −20 μA for 300 s) (the layout corresponds to Fig. 1*A*). (*F*) Direct concentration measurements of Ca^{2+} at the center of the ISM-coated contact ring during polarization with −20 μA for 300 s (the shaded region shows the SD; $n = 3$).

magnitude and duration of applied current primarily affect the extent of Ca^{2+} depletion rather than its effective volume.

We then subjected the ISM cuff to the direct concentration measurement technique that our group recently introduced (*Materials and Methods*) (27). Using this technique, we verified the behavior of the ISM-cuff system in terms of predictions from the transport model and monitored for the onset of adverse processes. As shown in Fig. 2*F*, we observed that each ISM-coated contact ($n = 3$), driving −20 μA of current, quickly reduced the Ca^{2+} concentration in the center of the ring from 2 to 0.5 mM within the first 100 s of its operation. The concentration leveled off at that point, maintaining a nearly constant level over the remainder of the first 5-min period and gradually returning toward equilibrium after the termination of current. We see that the onset of depletion occurs on a faster timescale than the model predicts, likely a consequence of convective mixing processes that are not captured by our modeling (30). However, most importantly, the predicted magnitude of depletion was closely reproduced by our direct measurements, and the regime we examined does not give rise to leaching or the elimination of transport selectivity.

Electrochemical Modulation of Rat Sciatic Nerves In Vivo. To study the operation of our ISM-cuff electrode, we performed a sequence of threshold search measurements on the sciatic nerve of a rat during the device's acute implantation in vivo (depicted in Fig. 3*A*). We aimed to determine whether the threshold of activation for downstream effectors of the sciatic nerve—the gastrocnemius, biceps femoris, and tibialis anterior—could be selectively modulated by driving the depletion of Ca^{2+} in the interstitial volume enclosed by the cuff, as illustrated schematically in Fig. 3*B*.

As shown in Fig. 3 *C–G*, we executed our protocol for studying the sensitivity of the rat sciatic nerve to electrical stimulation in 11 stages. Stages S2 to S6 correspond to our experimental group,

and stages S1 and S7 to S11 correspond to our controls. Our controls were executed both before and after the experimental group. We carried out each threshold search under the procedure discussed in *Materials and Methods*. Across all of our subjects, we found that, prior to Ca^{2+} depletion, the absolute thresholds for each contact were highly consistent. This allowed us to apply the same range of current pulses to each subject, −5 to −200 μA, while capturing both horizontal asymptotes of each recruitment curve. Looking at the latency between each stimulation pulse and the resulting CMAP, we observed minimal changes over the course of each experiment—the latency shifted by 0.2 ± 0.071 ms on average ($n = 7$) for the gastrocnemius channel (*SI Appendix*, Fig. S3 shows the average latency for each stage).

In our experimental group, Ca^{2+} depletion was performed under the verified operating conditions: −20 μA of current applied for 5 min. We did not observe spontaneous activity in any of the electromyographic (EMG) channels during the depletion of Ca^{2+}, consistent with the fact that the depletion current was substantially smaller than the lowest threshold we measured in all of our experiments. As shown in the representative recruitment curves in Fig. 4*B*, the activation threshold for each of the muscles we recorded from fell substantially after the depletion of interstitial Ca^{2+} (all recruitment curves can be found in *SI Appendix*, Fig. S4). Repeatedly, across all eight of our experiments, the ISM-cuff electrode reduced the thresholds of our subjects by $-49.3 \pm 11.6\%$ ($n = 8$), $-50.0 \pm 10.6\%$ ($n = 8$), and $-35.1 \pm 13.8\%$ ($n = 8$) relative to their levels in stage S2 for the gastrocnemius, biceps femoris, and tibialis anterior channels, respectively (Fig. 4*A*).

As shown in Fig. 2*F*, the concentration of Ca^{2+} gradually shifted back toward its original levels after the applied current was shut off. To understand how the threshold of the nerve evolved over the interval corresponding to 300 and 600 s in Fig. 2*F*, we carried out an additional threshold search (stage S6) after letting
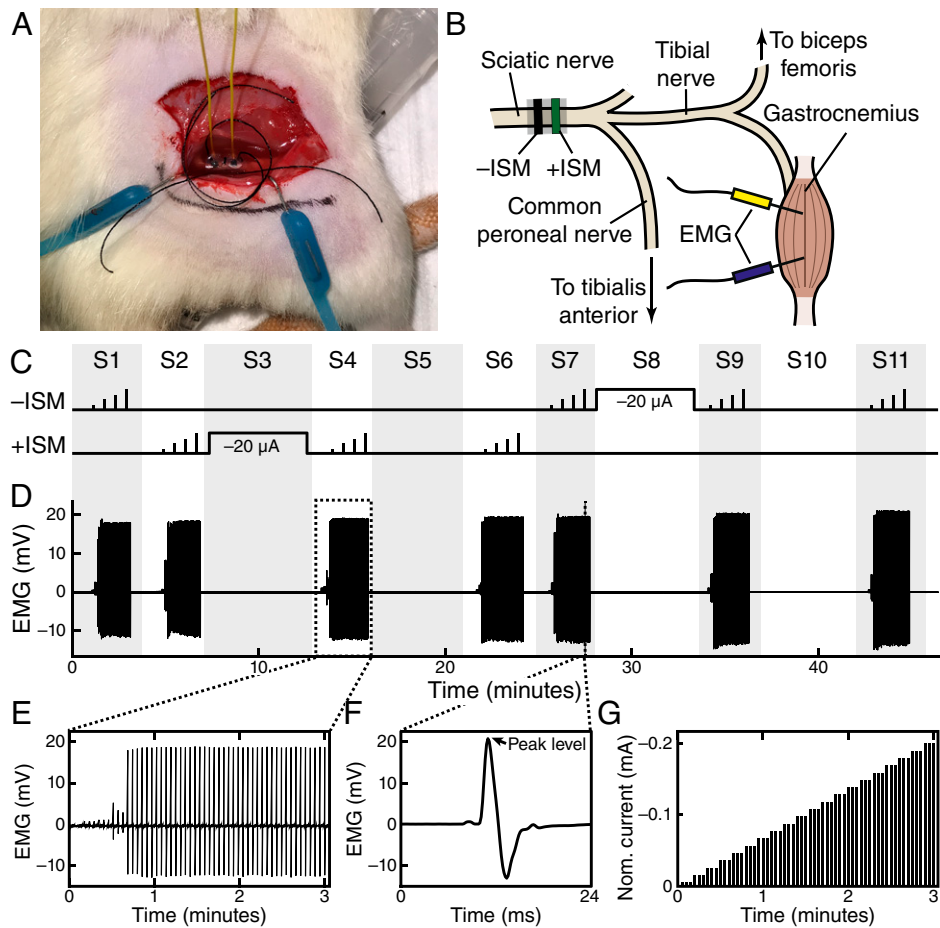
Fig. 3. Experimental setup for acute in vivo rat sciatic nerve studies. (*A*) Photograph of the ISM-cuff electrode taken immediately after implantation in one of our subjects and before the experimental protocol was executed. (*B*) Schematic illustration of nerve preparation, showing the locations of the cuff electrode and EMG needles with respect to the sciatic nerve and its branches. (*C*) Experimental protocol for the threshold measurements divided into 11 sequential stages. Each stage corresponds to a threshold search (wedge of vertical bars; 3-min duration), prolonged current (rectangular pulse; 5-min duration), or rest interval from either the ISM-coated contact (+ISM) or uncoated contact (−ISM; 5-min duration). (*D*) Raw EMG time series for the gastrocnemius recorded over the course of the entire experimental protocol. (*E*) A 3-min interval of the raw EMG reading spanning a single threshold search. (*F*) A narrow 0.4-ms interval of the raw EMG time series showing a single CMAP. The peak level (absolute value) used to construct the recruitment curves is indicated in this plot. (*G*) Nominal applied current during each of the threshold search stages.

the nerve rest for 5 min without current (stage S5). Fig. 4 *A* and *B* shows that the thresholds of each channel partially restored over the course of 5 min without any current, having shifted back toward the original level by 16.1% on average. Thus, the temporal change in the nerve's threshold was consistent with that of the underlying Ca^{2+} concentration.

In order to discount the confounding factor of prolonged direct current, whether this alone could affect the nerve's threshold, we implemented the controls corresponding to stages S7 to S11. The conditions of this sequence mirrored those of stages S2 to S6, with the exception that the prolonged current (−20 μA for 5 min) and threshold search were performed from the uncoated contact (−ISM). As shown in Fig. 4 *A* and *C*, the thresholds of our subjects' nerves changed by $-2.91 \pm 3.00\%$ ($n = 8$), $-2.18 \pm 1.92\%$ ($n = 8$), and $-1.54 \pm 2.49\%$ ($n = 8$) relative to their levels in stage S7 for the gastrocnemius, biceps femoris, and tibialis anterior channels, respectively. These relative changes are nearly negligible, and a statistically significant difference exists between them and those of our experimental group, satisfying $P < 0.001$. Thus, our results indicate that the reduction in threshold arises from driving current across the ISM and not the current itself.

In order to discount the possible effect of ambient processes changing the threshold of the nerve independently of our device's operation, we implemented the controls corresponding to stages

S1 and S7. In each of these stages, the threshold was determined for the uncoated contact (−ISM). Since the attributes of the nerve should remain unchanged beyond the narrow segment affected by Ca^{2+} depletion, the threshold measured from the uncoated contact should reflect independent factors, such as dehydration and changes in temperature, that could develop over time. As shown in Fig. 4 *A* and *C*, the thresholds of our subjects' nerves changed by $-5.55 \pm 3.61\%$ ($n = 7$), $-5.10 \pm 4.66\%$ ($n = 7$), and $-3.31 \pm 6.18\%$ ($n = 7$) relative to their levels in stage S1 for the gastrocnemius, biceps femoris, and tibialis anterior channels, respectively. Considering that these changes are relatively small with respect to those determined in our experimental group, we consider it unlikely that independent factors had a significant contribution to our perceived effect. The small reduction that we observed possibly indicates that Ca^{2+} depletion spread from the ISM-coated contact into the adjacent regions of the cuff, where it had a minor effect on the adjacent uncoated contact.

As shown in *SI Appendix*, Fig. S5, the ISM coating loses conductivity over the interval of Ca^{2+} depletion. To enable applications that have tighter restrictions on power, such as chronic stimulation, we evaluated an alternative configuration for multimodal stimulation. We carried out stages S1 to S7 under the same conditions as previously described, with the exception that the electrical stimulation applied for the threshold search
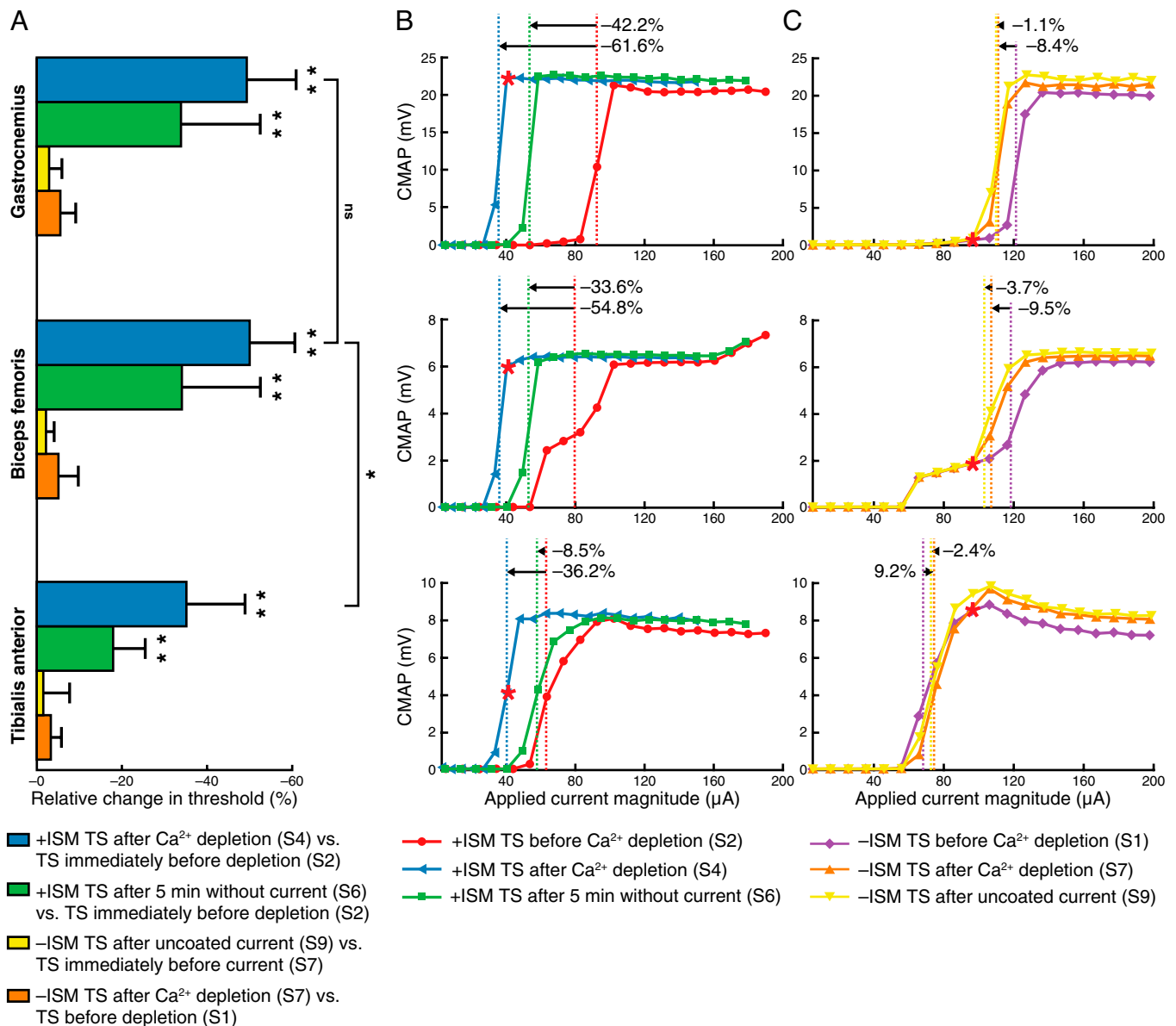
Fig. 4. Threshold search (TS) results for the gastrocnemius, biceps femoris, and tibialis anterior corresponding to *Top*, *Middle*, and *Bottom*, respectively, in *A–C*. (*A*) Relative changes in threshold before and after Ca^{2+} depletion (+ISM, coated electrode) and control manipulations (–ISM, uncoated electrode) measured across eight subjects. Thresholds were determined from recruitment curves exemplified in *B* and *C*. Ca^{2+} depletion was generated by applying $-20\,\mu A$ at the +ISM electrode. The first control (yellow) demonstrates the change in threshold measured at the –ISM electrode after applying $-20\,\mu A$ at the +ISM electrode. The second control (orange) demonstrates the change in threshold measured at the –ISM electrode after carrying out stages S2 to S6. For each channel, the relative changes in thresholds measured before vs. after Ca^{2+} depletion (stage S3) satisfied $**P < 0.001$ (based on the two-sample *t* test with the equal variance assumption) with respect to the relative changes that were induced before vs. after the current on the uncoated channel (stage S8). There was no statistically significant difference (ns; based on the two-sample *t* test with the equal variance assumption) observed between the gastrocnemius and biceps femoris channels both for the thresholds measured immediately after Ca^{2+} depletion (stage S4) and for the thresholds measured after 5 min without current (stage S6). Between both the gastrocnemius and tibialis anterior channels and the biceps femoris and tibialis anterior channels, there was a statistically significant difference, satisfying $*P < 0.05$ (based on the two-sample *t* test with the equal variance assumption) both for the thresholds measured immediately after Ca^{2+} depletion (stage S4) and for the thresholds measured after 5 min without current (stage S6). (*B*) Representative recruitment curves for subject 1 corresponding to the threshold measurements taken in our experimental group (stages S2, S4, and S6; $n = 8$). The red asterisks mark the CMAP amplitudes for a current pulse of magnitude 40.1 μA, highlighting the relative effect in each muscle for the ISM-coated contact. (*C*) Example recruitment curves for the same subject corresponding to the threshold measurements taken in our control groups (stages S1, S7, and S9; $n = 8$ for stages S7 and S9 and $n = 7$ for stage S1). The red asterisks mark the CMAP amplitudes for a current pulse of magnitude 96 μA, highlighting the relative effect in each muscle for the uncoated contact.

in stages S2 and S4 was delivered with an auxiliary electrode: a thin-gauge platinum wire wrapped in between the nerve and the ISM-coated contact. As demonstrated by the recruitment curves in *SI Appendix*, Fig. S5, the depletion of Ca^{2+} produced behavior matching that observed from the original configuration—the thresholds of the nerve changed by -16.1, -14.4, and $-1.02\,\%$ relative to their levels in stage S2 for the gastrocnemius, biceps femoris, and tibialis anterior, respectively. Driving electrical

stimulation through the low-impedance platinum wire rather than the ISM-coated contact, this configuration succeeded in lowering the threshold while sourcing less power in each pulse of stimulation.

As demonstrated in Fig. 4, while there was no statistically significant difference between the activation thresholds of the gastrocnemius and biceps femoris, a significant difference did exist between those muscles and the tibialis anterior, satisfying

$P < 0.05$. Furthermore, this difference can be seen in the low-power configuration with the auxiliary electrode. These results reflect the underlying anatomy of the system—the biceps femoris and gastrocnemius are both innervated by the tibial branch of the sciatic nerve, while the tibialis anterior is innervated by the common peroneal branch. Our results strongly suggest that Ca^{2+} depletion had a significantly larger effect on the tibial branch compared with the common peroneal branch.

Discussion

Leveraging the confined volume created by the insulated body of the cuff, we designed a multimodal stimulator that could control Ca^{2+} concentrations within a targeted region. We verified the behavior of this system in the context of predictions from a theoretical transport model using direct concentration measurements. Using this methodology, we showed that an ISM electrode embedded in an implantable cuff could be operated without encountering adverse processes, such as selectivity loss and leaching of membrane components (27).

Implanted on the rat sciatic nerve in an in vivo environment, we demonstrated that our Ca^{2+}-selective ISM-cuff electrode could reduce thresholds to a far greater extent than our control groups. This demonstration of the effect of Ca^{2+} depletion in such a model agrees with the ex vivo results reported by Song et al. (15).

In our controls, we observed that prolonged current applied at an uncoated electrode was insufficient to elicit a change in the nerve's threshold. Comparing this threshold from the uncoated channel (stage S7) with the threshold measured on the same channel at the beginning of the experiment (stage S1), we observed only a small reduction. This change may have arisen from some overlap between the affected volumes of excitatory current applied at the uncoated channel during stage S7 and Ca^{2+} depletion (generated in stage S3) diffusing longitudinally away from the ISM-coated channel. Ultimately, the effects of each channel were sufficiently independent that we could clearly see differences in their influence on the three muscles we recorded from.

We provided evidence that the effect of ion modulation could selectively influence individual fascicles within the nerve. Supporting our initial hypothesis, Fig. 4 demonstrated that Ca^{2+} depletion had differential effects on the common peroneal and tibial branches of the sciatic nerve. Factoring in relative differences in the initial thresholds, we selectively activated the gastrocnemius over the tibialis anterior in four of eight of our subjects after Ca^{2+} depletion. In the subject shown in Fig. 4, stimulating the nerve at $-40.1\,\mu A$ after Ca^{2+} depletion allowed us to excite the gastrocnemius selectively to 100% of its maximal level while activating the tibialis anterior to only 50% of its maximal level (illustrated by the red asterisks in Fig. 4*B*). Simultaneously, by stimulating the nerve at $-96.0\,\mu A$ on the uncoated contact, we were able to excite the tibialis anterior selectively to 100% of its maximal level while activating the gastrocnemius to only 3.3% of its maximal level (illustrated by the red asterisks in Fig. 4*C*).

As part of a clinical modality, such as VNS, the optimal targets would first need to be identified in terms of the differential effects of Ca^{2+}. In coordination with repetitive (31, 32) or on-demand (33) electrical stimulation, those effects could then be leveraged to deliver the behaviors illustrated in Fig. 4. As discussed by Aristovich et al. (5), this functional selectivity may alleviate some of the side effects currently associated with VNS.

The basis for the selective behavior we observed may be the morphological differences between the fascicles of the sciatic nerve. The diameter of the fascicle that diverges into the common peroneal nerve is smaller than the tibial nerve's respective fascicle, and fibers branching into the common peroneal nerve are narrower, on average, than those leading to the tibial nerve (25, 34). This may give rise to differences in transport characteristics, such as ionic diffusivity, between the nerve fascicles (24). Electrical stimulation has been shown to stimulate large-diameter nerves with a lower threshold (35), and a similar principle may contribute to the effect we saw for Ca^{2+} depletion.

Furthermore, the differences in axon diameter may correlate with variations in the gene expression of voltage-gated sodium channels. The activities of these channels are intrinsically linked to the firing threshold of a nerve (23). Ten varieties of voltage-gated sodium channels are currently known (36, 37), and previous studies have reported preferential expression of these subtypes in axons of specific sizes (38–40). Considering that the effect of Ca^{2+} modulation mechanistically involves voltage-gated sodium channels (22) and that the influence of Ca^{2+} on these channels may preferentially affect particular subtypes (41), differential expression could be another contributing factor to the selectivity of electrochemical modulation. Further investigation to isolate the specific origins of functional selectivity would be valuable, and our platform offers a tailored approach for studying these phenomena.

Through these mechanisms, electrochemical modulation potentially offers an approach for exerting selective control with an electrical neuroprosthetic device. Furthermore, it can be used together with existing approaches, such as spatially resolved electrode arrays. Like electrical stimulation, the resolution of electrochemical modulation scales with electrode size. At the expense of invasiveness, one could adapt the ISM coating to subfascicular contacts ($\sim100\,\mu m$) by fabricating them as part of a penetrating electrode (42). Mean fascicular diameters are $\sim500\,\mu m$ for mammalian sciatic nerves (25) and $\sim200\,\mu m$ for mammalian vagus nerves (43).

Therapeutic applications, such as VNS, require that implanted devices remain stable over long periods of operation. Peripheral nerve implants can perform continuously over durations exceeding 10 y (44). Although longitudinal data on ISM stability have not been established, previous investigators have found that ISM-based sensors retain their performances beyond 86 d in vivo (45, 46). According to theoretical estimates, the lifetimes of membrane components in optimized ISM-based sensors are on the order of years (47). Most common membrane components also demonstrate favorable results in cytotoxicity assays (48). Meanwhile, the operation required for electrochemical modulation may present additional limitations; in our previous work, we showed that electrical current can drive membrane components to escape under certain conditions (27). In the present study, we applied the same methodology with our direct concentration measurements and found no evidence of limiting behavior during operation of the ISM cuff (Fig. 2*F*).

Along with Ca^{2+}, this platform is compatible with a broad range of pharmacologically active ions, including K^+ and Mg^{2+}. K^+ produces a nerve block, which may enable treatments for pathological pain disorders (49). Mg^{2+} suppresses synaptic activity and has the potential to treat drug-resistant epilepsy (50, 51). Through similar mechanisms as Ca^{2+}, these ions may also elicit selective effects.

We report that Ca^{2+} depletion, as part of a multimodal system, offers enhanced functional selectivity and may, with further development, augment therapeutic modalities, such as VNS. The ISM raises the prospects of remote, spatially resolved, low-latency ion modulation and with remote refilling, does not suffer from

the intrinsic limitation of finite stock. Compatible with a wide range of pharmacologically active ions, it offers much broader functionality than direct electrical stimulation. Our results provide further demonstration of the viability of this approach for peripheral neuromodulation.

Materials and Methods

Fabrication of Cuff Electrodes. The cuff electrodes were adapted from the procedure introduced in ref. 27. We started with an 8-mm section of silicone tubing (Versilon SPX-50; 1.6-mm inner diameter, 3.2-mm outer diameter) as our substrate, opening it with a longitudinal cut. To pattern the contacts, we flattened the tubing exterior down against a glass slide using a piece of polyimide tape with silicone adhesive (1 Mil Kapton tape; Dupont). Using a computer numerical control laser cutter (PLS4.75; Universal Laser Systems), we then aligned and cut shallow channels through the tape and into the substrate according to a drawing of our intended electrode configuration. As shown in Fig. 1A, the electrode contacts were each patterned as three large 1.3×1.4 mm^2 pads interconnected by narrow 0.5×0.75 mm^2 (6.21 mm^2 total area) tracts. Similar to the split-contact electrodes discussed in ref. 52, the purpose of this design was to minimize deformations in the electrode contacts.

We then released the substrate from the glass slide, leaving the polyimide tape on the interior surface to act as a stencil. In order to hold the tubing in the open position, another layer of polyimide adhesive was applied onto the outer surface. In this position, insulated lead wires (30-gauge solid-core copper wires) were inserted through the outer surface of the substrate so that exposed wires (0.5 to 1 mm) were accessible on the inside in the center of each contact. We fixed the wires in place by coating two-part epoxy resin at the joint between the wire and the outer surface of the substrate and silver-filled epoxy at the joint between the wire and the inner surface. By covering the entire surface of the exposed wires in the interior of the cuff, the silver epoxy served as an additional barrier between the wires and electrolyte media.

After curing the epoxy resins holding the lead wires in place, we screen printed a conductive carbon composite (BQ242; Dupont) onto the inner surface of the substrate using the laser-patterned polyimide as a stencil. We wetted one of the carbon composite contacts with tetrahydrofuran and then, drop cast the ISM mixture onto it with an initial volume of 6 to 10 μL. Upon evaporation of the tetrahydrofuran, the ISM had a thickness of approximately 100 μm.

With the electrode contacts fully prepared, we released the substrate from the polyimide adhesive, allowing it to return to its cylindrical shape. Finally, we encapsulated the epoxy joints on the outer surface of the cuff with single-component silicone (3140 RTV; Dow Corning).

ISM Composition. Calcium ISMs were prepared in a conventional manner (16). This particular composition creates a high density of charge sites, which increases the membrane's conductivity. We created a mixture, which by weight, contained 4.3% ETH 129, 0.86% sodium tetraphenylborate, 80.84% 2-nitrophenyl octyl ether, and 14.0% high–molecular weight polyvinyl chloride. Then, we diluted this mixture in distilled tetrahydrofuran in a ratio of 1:3 by mass. All chemicals used for these membranes were Selectophore products purchased from Sigma Aldrich.

Electrochemical Characterization. We performed electrochemical impedance spectroscopy, cyclic voltammetry, and chronopotentiometry with the VersaSTAT 3 potentiostat from Princeton Applied Research. All devices were cleaned with isopropanol before testing. In each modality, our electrochemical cell comprised three electrodes immersed in room temperature phosphate buffered saline (1× PBS, pH 7.4): one of the cuff's cathodes as the working electrode, an Ag–AgCl–3 M KCl cell as the reference electrode (grounded to the enclosing Faraday cage to reduce noise), and a 1- × 2-cm^2 section of carbon paper (Spectracarb 2050A-0550; Fuel Cell Store) as the counter electrode. For each electrode evaluated, we performed all measurements before and after repeatedly opening/closing the cuff (three times by 2 mm, consistent with the surgical implantation) in order to test mechanical properties.

Physicochemical Transport Modeling. We modeled solute transport in the inner volume of the cuff electrode according to Nernst–Planck–Poisson in

cylindrical coordinates with a two-dimensional axisymmetric geometry. We treated the intramembrane processes as being in quasiequilibrium, with its variables solved according to an analytical phase-boundary model. Additional details, including boundary conditions and parameter values, are in *SI Appendix*.

Direct Concentration Measurements. We carried out direct concentration measurements using the source–measurement time-share method recently introduced in ref. 27. The purpose of these experiments was to measure the concentration of Ca^{2+} in the aqueous diffusion boundary layer adjacent to the ISM-coated contact of our cuffs. We would position a probe inside the region of interest using micromanipulators under a microscope. In this case, the probe was a glass micropipette with a Ca^{2+}-selective ISM embedded in the tip. Using zero-current potentiometry, we would measure the concentration of Ca^{2+} using the probe while current was applied across the ISM-coated contact. Additional details are in *SI Appendix*.

Surgical Preparation of Rat Sciatic Nerve and Implantation. We carried out all animal procedures under the guidelines of the Committee on Animal Care at the Massachusetts Institute of Technology, minimizing pain experienced by the rats. Surgical exposure of the sciatic nerve followed a similar protocol to those described in the literature, such as those in refs. 23–25.

The rat was anesthetized using a mixture of ketamine/xylazine/acepromazine (1:0.125:0.01 ratio by mass). We administered an initial dose of 0.1 mL per 100 g of the rat's body weight intraperitoneally through the lower right abdominal area. After 1 h, successive doses at half-volume were injected in 45-min intervals. We completed each surgery and implantation within 40 to 50 min of the initial dosage of anesthesia. The experiment would begin at 60 min from the time of initial dosage, following a single maintenance dose that would last for the duration of the procedure.

We positioned the rat on its abdominal side over a 37 °C heating pad to maintain physiological temperature. To expose the sciatic nerve, we separated the femoral biceps and gluteal muscles by blunt dissection. We dissected the sciatic nerve from the surrounding connective tissue along the lateral aspect of the limb (~2.5 cm, leaving room for slightly more than two lengths of the cuff). Before implantation, we lightly irrigated the tissue and wetted the inside surface of the ISM-cuff electrode with Ringer's lactate solution. We wrapped the cuff around the main branch of the sciatic nerve proximal to its trifurcation, affixing sutures around the device to seal the opening. Finally, the wound was closed by suturing the skin with one layer of 5-0 Prolene surgical knots, leaving percutaneous leads for amplifier connection.

Threshold Search with EMG Recordings. To quantify changes in firing characteristics of the sciatic nerve, we performed intramuscular EMG recordings on three of its downstream targets: the gastrocnemius, tibialis anterior, and biceps femoris muscles. CMAPs, which reflect upstream activity of innervating fibers, were recorded from pairs of stainless steel EMG needles inserted into each muscle with gaps of ~1 cm. With a differential amplifier (PZ2 amplifier; Tucker–Davis Technologies; sampled at 6.1 kHz), we acquired each channel vs. a distant reference needle inserted into the latissimus dorsi muscle (~10 cm from the nerve exposure).

We recorded each channel simultaneously for the entire duration of the experiment throughout threshold search, prolonged current, and nontreatment stages of the protocol. In the threshold search and prolonged current stages, the current was driven through either the ISM-coated or uncoated contact in a monopolar configuration from a current-controlled amplifier (2612B SourceMeter; Keithley). For each contact, a stainless steel EMG needle inserted into the latissimus dorsi muscle (separate from the EMG reference) served as the grounded return for the current. In the prolonged current stages, the instrument supplied a constant current of −20 μA for 5 min. In the threshold search stages, it applied a ramp of pulses, increasing in magnitude linearly over time. Each ramp consisted of 20 steps spaced evenly between –5 and −200 μA (nominal applied current), and each step consisted of three 1-ms monophasic pulses triggered 3 s apart. The SourceMeter unit recorded the actual currents applied in each of these pulses, which differed from the nominal levels in cases where the electrode impedance was high.

For each pulse driven through the cuff electrode in the threshold search stages, we quantified the downstream activation of each muscle by the peak-rectified amplitude of the elicited CMAP. We constructed recruitment curves by averaging the triplicate pulses from each step and plotting them vs. the actual stimulus amplitude at that step. Finally, we calculated the thresholds as the current at which the recruitment curve reached 50% of its maximal level (linearly interpolated). All postprocessing was performed in MATLAB from MathWorks and the Julia programming language.

Data Availability. Raw data have been deposited in Open Science Framework (https://osf.io/hfdnx/) (53).

Author affiliations: ᵃDepartment of Electrical Engineering & Computer Science, Massachusetts Institute of Technology, Cambridge, MA 02139; ᵇBioengineering Division, Draper, Cambridge, MA 02139; ᶜDivision of Plastic and Reconstructive Surgery, Department of Surgery, Beth Israel Deaconess Medical Center, Harvard Medical School, Boston, MA 02215; ᵈDepartment of Plastic Surgery, Lower Silesia Specialist Hospital, 54-049 Wroclaw, Poland; ᵉMcGovern Institute for Brain Research, Massachusetts Institute of Technology, Cambridge, MA 02139; and ᶠDepartment of Biological Engineering, Massachusetts Institute of Technology, Cambridge, MA 02139

1. S. M. Won, E. Song, J. T. Reeder, J. A. Rogers, Emerging modalities and implantable technologies for neuromodulation. *Cell* **181**, 115–135 (2020).
2. D. J. Englot, E. F. Chang, K. I. Auguste, Vagus nerve stimulation for epilepsy: A meta-analysis of efficacy and predictors of response. *J. Neurosurg.* **115**, 1248–1255 (2011).
3. S. M. Berry et al., A patient-level meta-analysis of studies evaluating vagus nerve stimulation therapy for treatment-resistant depression. *Med Devices (Auckl).* **6**, 17–35 (2013).
4. J. H. Burridge et al., Phase II trial to evaluate the ActiGait implanted drop-foot stimulator in established hemiplegia. *J. Rehabil. Med.* **39**, 212–218 (2007).
5. K. Aristovich et al., Model-based geometrical optimisation and in vivo validation of a spatially selective multielectrode cuff array for vagus nerve neuromodulation. *J. Neurosci. Methods* **352**, 109079 (2021).
6. E. Ben-Menachem, Vagus nerve stimulation, side effects, and long-term safety. *J Clin. Neurophysiol.* **18**, 415–418 (2001).
7. W. M. Grill, S. E. Norman, R. V. Bellamkonda, Implanted neural interfaces: Biochallenges and engineered solutions. *Annu. Rev. Biomed Eng.* **11**, 1–24 (2009).
8. K. H. Polasek, H. A. Hoyen, M. W. Keith, R. F. Kirsch, D. J. Tyler, Stimulation stability and selectivity of chronically implanted multicontact nerve cuff electrodes in the human upper extremity. *IEEE Trans. Neural Syst. Rehabil. Eng.* **17**, 428–437 (2009).
9. C. E. Larson, E. Meng, A review for the peripheral nerve interface designer. *J. Neurosci. Methods* **332**, 108523 (2020).
10. A. H. C. Vlot et al., Target and tissue selectivity prediction by integrated mechanistic pharmacokinetic-target binding and quantitative structure activity modeling. *AAPS J.* **20**, 11 (2017).
11. C. B. Weldon et al., Electrospun drug-eluting sutures for local anesthesia. *J. Control. Release* **161**, 903–909 (2012).
12. A. M. Cobo et al., Parylene-based cuff electrode with integrated microfluidics for peripheral nerve recording, stimulation, and drug delivery. *J. Microelectromech. Syst.* **28**, 36–49 (2019).
13. A. Jonsson et al., Therapy using implanted organic bioelectronics. *Sci. Adv.* **1**, e1500039 (2015).
14. D. T. Simon, E. O. Gabrielsson, K. Tybrandt, M. Berggren, Organic bioelectronics: Bridging the signaling gap between biology and technology. *Chem. Rev.* **116**, 13009–13041 (2016).
15. Y. A. Song et al., Electrochemical activation and inhibition of neuromuscular systems through modulation of ion concentrations with ion-selective membranes. *Nat. Mater.* **10**, 980–986 (2011).
16. E. Bakker, P. Bühlmann, E. Pretsch, Carrier-based ion-selective electrodes and bulk optodes. 1. General characteristics. *Chem. Rev.* **97**, 3083–3132 (1997).
17. Z. Samec, Dynamic electrochemistry at the interface between two immiscible electrolytes. *Electrochimica Acta* **84**, 21–28 (2012).
18. E. Grygolowicz-Pawlak, E. Bakker, Thin layer coulometry with ionophore based ion-selective membranes. *Anal. Chem.* **82**, 4537–4542 (2010).
19. M. Ghahraman Afshar, G. A. Crespo, E. Bakker, Direct ion speciation analysis with ion-selective membranes operated in a sequential potentiometric/time resolved chronopotentiometric sensing mode. *Anal. Chem.* **84**, 8813–8821 (2012).
20. V. V. Nikonenko et al., Intensive current transfer in membrane systems: Modelling, mechanisms and application in electrodialysis. *Adv. Colloid Interface Sci.* **160**, 101–123 (2010).
21. F. Brink Jr., D. W. Bronk, M. G. Larrabee, Chemical excitation of nerve. *Ann. N. Y. Acad. Sci.* **47**, 457–485 (1946).
22. C. M. Armstrong, G. Cota, Calcium ion as a cofactor in Na channel gating. *Proc. Natl. Acad. Sci. U.S.A.* **88**, 6528–6531 (1991).
23. F. Yang et al., Differential expression of voltage-gated sodium channels in afferent neurons renders selective neural block by ionic direct current. *Sci. Adv.* **4**, eaaq1438 (2018).
24. N. G. Simon, J. Lagopoulos, T. Gallagher, M. Kliot, M. C. Kiernan, Peripheral nerve diffusion tensor imaging is reliable and reproducible. *J. Magn. Reson. Imaging* **43**, 962–969 (2016).
25. S. Ugrenović et al., *Morphological and Morphometric Analysis of Fascicular Structure of Tibial and Common Peroneal Nerves* (Medicine & Biology Series, Facta Universitatis, 2014), vol. 16, pp. 18–22.
26. M. T. Flavin, D. K. Freeman, J. Han, Interfacial ion transfer and current limiting in neutral-carrier ion-selective membranes: A detailed numerical model. *J. Membr. Sci.* **572**, 374–381 (2019).
27. M. T. Flavin, "Electrochemical modulation of peripheral nerves using ion-selective electrodes," doctoral thesis, Massachusetts Institute of Technology, Cambridge, MA (2021).
28. M. T. Flavin et al., Rapid and low cost manufacturing of cuff electrodes. *Front. Neurosci.* **15**, 628778 (2021).
29. S. F. Cogan, Neural stimulation and recording electrodes. *Annu. Rev. Biomed Eng.* **10**, 275–309 (2008).
30. C. Amatore, S. Szunerits, L. Thouin, J. S. Warkocz, The real meaning of Nernst's steady diffusion layer concept under non-forced hydrodynamic conditions. A simple model based on Levich's seminal view of convection. *J. Electroanal. Chem. (Lausanne)* **500**, 62–70 (2001).
31. R. McLachlan, Vagus nerve stimulation for intractable epilepsy: A review. *J. Clin. Neurophysiol.* **14**, 358–368 (1997).
32. F. A. Koopman et al., Vagus nerve stimulation inhibits cytokine production and attenuates disease severity in rheumatoid arthritis. *Proc. Natl. Acad. Sci. U.S.A.* **113**, 8284–8289 (2016).
33. J. Dawson et al., Safety, feasibility, and efficacy of vagus nerve stimulation paired with upper-limb rehabilitation after ischemic stroke. *Stroke* **47**, 143–150 (2016).
34. J. E. Swett, R. P. Wikholm, R. H. Blanks, A. L. Swett, L. C. Conley, Motoneurons of the rat sciatic nerve. *Exp. Neurol.* **93**, 227–252 (1986).
35. E. Henneman, Relation between size of neurons and their susceptibility to discharge. *Science* **126**, 1345–1347 (1957).
36. N. Eijkelkamp et al., Neurological perspectives on voltage-gated sodium channels. *Brain* **135**, 2585–2612 (2012).
37. A. L. Goldin et al., Nomenclature of voltage-gated sodium channels. *Neuron* **28**, 365–368 (2000).
38. J. A. Black et al., Spinal sensory neurons express multiple sodium channel alpha-subunit mRNAs. *Brain Res. Mol. Brain Res.* **43**, 117–131 (1996).
39. T. R. Cummins, P. L. Sheets, S. G. Waxman, The roles of sodium channels in nociception: Implications for mechanisms of pain. *Pain* **131**, 243–257 (2007).
40. C. G. Faber et al., Gain of function Naᵥ1.7 mutations in idiopathic small fiber neuropathy. *Ann. Neurol.* **71**, 26–39 (2012).
41. L. Ferrera, O. Moran, Beta1-subunit modulates the Nav1.4 sodium channel by changing the surface charge. *Exp. Brain Res.* **172**, 139–150 (2006).
42. A. Cutrone et al., A three-dimensional self-opening intraneural peripheral interface (SELINE). *J. Neural Eng.* **12**, 016016 (2015).
43. N. A. Pelot et al., Quantified morphology of the cervical and subdiaphragmatic vagus nerves of human, pig, and rat. *Front. Neurosci.* **14**, 601479 (2020).
44. B. P. Christie et al., Long-term stability of stimulating spiral nerve cuff electrodes on human peripheral nerves. *J. Neuroeng. Rehabil.* **14**, 70 (2017).
45. C. Somps et al., Electrochemical performance of an ion selective, polymeric membrane following chronic implantation in rat subcutaneous tissue. *Sens. Actuators B Chem.* **35**, 222–227 (1996).
46. C. J. Somps, M. J. Madou, J. W. Hines, "Microfabricated electrochemical sensors for chronic physiologic monitoring" in *Biomedical Sensing and Imaging Technologies*, R. A. Lieberman, T. Vo-Dinh, Eds. (International Society for Optics and Photonics, SPIE, 1998), **vol. 3253**, pp. 199–207.
47. U. Oesch, W. Simon, Lifetime of neutral carrier based ion-selective liquid-membrane electrodes. *Anal. Chem.* **52**, 692–700 (1980).
48. R. Cánovas, S. Padrell Sánchez, M. Parrilla, M. Cuartero, G. A. Crespo, Cytotoxicity study of ionophore-based membranes: Toward on-body and in vivo ion sensing. *ACS Sens.* **4**, 2524–2535 (2019).
49. J. M. Peacock, R. Orchardson, Effects of potassium ions on action potential conduction in A- and C-fibers of rat spinal nerves. *J. Dent. Res.* **74**, 634–641 (1995).
50. D. B. Cotton, M. Hallak, C. Janusz, S. M. Irtenkauf, R. F. Berman, Central anticonvulsant effects of magnesium sulfate on N-methyl-D-aspartate-induced seizures. *Am. J. Obstet. Gynecol.* **168**, 974–978 (1993).
51. M. Hallak, R. F. Berman, S. M. Irtenkauf, M. I. Evans, D. B. Cotton, Peripheral magnesium sulfate enters the brain and increases the threshold for hippocampal seizures in rats. *Am. J. Obstet. Gynecol.* **167**, 1605–1610 (1992).
52. J. S. Ordonez et al., "Cuff electrodes for very small diameter nerves: Prototyping and first recordings in vivo" in *2014 36th Annual International Conference of the IEEE Engineering in Medicine and Biology Society, EMBC 2014* (IEEE, 2014), pp. 6846–6849.
53. M. T. Flavin et al., Electrochemical modulation enhances the selectivity of peripheral neuro-stimulation in vivo. Open Science Framework. https://osf.io/hfdnx/. Deposited 16 February 2022.